



# Macrophage membrane-biomimetic adhesive polycaprolactone nanocamptothecin for improving cancer-targeting efficiency and impairing metastasis

Kangkang Ying<sup>a,b,d</sup>, Yifeng Zhu<sup>c</sup>, Jianqin Wan<sup>a</sup>, Chenyue Zhan<sup>a</sup>, Yuchen Wang<sup>a,e</sup>, Binbin Xie<sup>d,\*\*</sup>, Peirong Xu<sup>a,e</sup>, Hongming Pan<sup>d</sup>, Hangxiang Wang<sup>a,b,c,\*</sup>

<sup>a</sup> The First Affiliated Hospital, NHC Key Laboratory of Combined Multi-Organ Transplantation, Zhejiang University School of Medicine, Hangzhou, Zhejiang Province, 310003, PR China

<sup>b</sup> Jinan Microecological Biomedicine Shandong Laboratory, Jinan, Shandong Province, 250117, PR China

<sup>c</sup> Department of Hepatobiliary Surgery, The First Affiliated Hospital, Wenzhou Medical University, Wenzhou, Zhejiang Province, 325000, PR China

<sup>d</sup> Department of Medical Oncology, Sir Run Run Shaw Hospital, Zhejiang University School of Medicine, Hangzhou, Zhejiang Province, 310016, PR China

<sup>e</sup> Department of Chemical Engineering, Zhejiang University, Hangzhou, Zhejiang Province, 310027, PR China

## ARTICLE INFO

### Keywords:

Polymer prodrug  
Macrophage membrane  
Cancer nanomedicine  
Antimetastasis  
Nanocamptothecin

## ABSTRACT

The recent remarkable success and safety of mRNA lipid nanoparticle technology for producing severe acute respiratory syndrome coronavirus 2 (SARS-CoV-2) vaccines has stimulated intensive efforts to expand nanoparticle strategies to treat various diseases. Numerous synthetic nanoparticles have been developed for pharmaceutical delivery and cancer treatment. However, only a limited number of nanotherapies have entered clinical trials or are clinically approved. Systemically administered nanotherapies are likely to be sequestered by host mononuclear phagocyte system (MPS), resulting in suboptimal pharmacokinetics and insufficient drug concentrations in tumors. Bioinspired drug-delivery formulations have emerged as an alternative approach to evade the MPS and show potential to improve drug therapeutic efficacy. Here we developed a biodegradable polymer-conjugated camptothecin prodrug encapsulated in the plasma membrane of lipopolysaccharide-stimulated macrophages. Polymer conjugation revived the parent camptothecin agent (e.g., 7-ethyl-10-hydroxy-camptothecin), enabling lipid nanoparticle encapsulation. Furthermore, macrophage membrane cloaking transformed the nonadhesive lipid nanoparticles into bioadhesive nanocamptothecin, increasing the cellular uptake and tumorigenic effects of this biomimetic therapy. When tested in a preclinical murine model of breast cancer, macrophage-camouflaged nanocamptothecin exhibited a higher level of tumor accumulation than uncoated nanoparticles. Furthermore, intravenous administration of the therapy effectively suppressed tumor growth and the metastatic burden without causing systematic toxicity. Our study describes a combinatorial strategy that uses polymeric prodrug design and cell membrane cloaking to achieve therapeutics with high efficacy and low toxicity. This approach might also be generally applicable to formulate other therapeutic candidates that are not compatible or miscible with biomimetic delivery carriers.

## 1. Introduction

The recent remarkable success of mRNA lipid nanoparticles in developing innovative severe acute respiratory syndrome coronavirus 2 (SARS-CoV-2) vaccines has stimulated intensive efforts to develop nanotechnology strategies to address various unmet medical needs [1,

2]. In particular, cancer nanomedicines are envisioned as magic bullets, travelling through the blood circulation to target tumors while limiting their access to healthy organs. Compared with conventional free therapeutics, nanomedicines have the potential to increase the duration, bioavailability, and efficacy, as well as to minimize systemic side effects [3,4]. However, systemically administered nanotherapies are likely to

Peer review under responsibility of KeAi Communications Co., Ltd.

\* Corresponding authors. The First Affiliated Hospital, Zhejiang University School of Medicine; 79, Qingchun Road, Hangzhou, 310003, China.

\*\* Corresponding authors.

E-mail addresses: [xieBB@zju.edu.cn](mailto:xieBB@zju.edu.cn) (B. Xie), [wanghx@zju.edu.cn](mailto:wanghx@zju.edu.cn) (H. Wang).

<https://doi.org/10.1016/j.bioactmat.2022.06.013>

Received 26 January 2022; Received in revised form 3 May 2022; Accepted 15 June 2022

2452-199X/© 2022 The Authors. Publishing services by Elsevier B.V. on behalf of KeAi Communications Co. Ltd. This is an open access article under the CC BY-NC-ND license (<http://creativecommons.org/licenses/by-nc-nd/4.0/>).

be sequestered by the host mononuclear phagocyte system (MPS), resulting in suboptimal pharmacokinetics and insufficient intratumor drug accumulation [5,6]. Extensive efforts have been made to develop surface cloaking strategies to extend the circulation time of therapeutic nanoparticles. Synthetic polymers such as poly(ethylene glycol) (PEG), poly(L-glutamic acid), or zwitterionic polymers are popularly used for this purpose [7,8]. Notwithstanding the originally envisioned inertness, exogenous PEGylated nanoparticles are also reported to potentially activate innate immunity and are readily cleared from the blood circulation, thereby compromising their efficacy and failing to reduce side effects [9–12].

In this regard, interest in developing biomimetic cell membrane-cloaked platforms to potentiate the use of nanomedicines for biomedical applications is increasing [13–15]. These biomimetic nanosystems are composed of a synthetic nanoparticle core and wrapped natural cell membranes at the periphery. Due to the preserved membrane compositions and antigens, some unique features and functions are inherited in these systems, including specific neutralization of pathological molecules, immune escape capability, prolonged blood circulation, and homing to disease lesions. In this context, various cell types have been proposed as sources to prepare membrane-cloaked nanotherapies [16], including red blood cells (RBCs) [13], white blood cells (WBCs) [17], platelets [14], cancer cells [18,19], and stem cells [20,21]. Bacteria-derived outer membrane vesicles [21] and cell-derived extracellular vesicles were also used for nanoparticle modification to create biomimetic drug delivery systems [22]. Among these cell types, exploiting immune cell membranes to generate biomimetic platforms has attracted particular attention. Macrophages, which are bone marrow-derived leucocytes, sense chemotactic cues and have the capacity to navigate to tumors with high efficiency [23]. In addition to this tumor-tropic effect, macrophages are also reported to penetrate hypoxic areas of tumors that lack blood vessels and are inaccessible to conventional chemotherapies. Hence, these unique characteristics render the macrophage membrane a potentially appealing biomimetic carrier for cancer drug delivery.

Therapeutic agents are generally encapsulated within cell membrane-cloaked nanocarriers via noncovalent approaches [24,25]. However, physically entrapped drugs are readily liberated from the delivery platforms, resulting in rapid drug metabolism and poor pharmacokinetic properties. In addition, burst release of toxic chemotherapeutic drugs in the blood circulation eventually leads to undesired systemic side effects [26]. Prodrugs are temporarily inactive molecules that are converted to the active parent drug *in vivo* through enzymatic and/or chemical reaction-triggered bond cleavage. Through the modification of fundamental moieties, physicochemical properties or *in vivo* performance might be substantially improved relative to the parent drugs. We previously showed that the anticancer agent 7-ethyl-10-hydroxy-camptothecin (SN38) is reversibly ligated to poly( $\epsilon$ -caprolactone (PCL) via an ester bond to generate the new prodrug entities (i.e., PCL-SN38). The resulting prodrugs are readily assembled in poly(ethylene glycol)-*block*-poly( $\epsilon$ -caprolactone) copolymers (e.g., PEG<sub>10k</sub>-*b*-PCL<sub>10k</sub>) to form systemically injectable nanotherapies [27]. With re-engineered drug molecules, the miscibility and compatibility of the prodrugs with the delivery matrices are increased, while the nanoparticle reservoirs exhibit esterase-responsive release of active SN38 agents. Consequently, this approach attenuates the toxicity of chemotherapies, and drugs can be injected at higher doses.

By taking advantage of biomimetic membrane-camouflaged formulations and polymeric prodrug strategies, we propose a facile approach to potentiate anticancer chemotherapy in the present study. Our approach is based on polymeric SN38 lipid nanoparticles (referred to as SLP), with further surface cloaking with cell membranes derived from a lipopolysaccharide (LPS)-stimulated murine monocyte/macrophage cell line, resulting in the formulation of M1-type macrophage membrane-cloaked cytotoxic nanocamptothecin therapy (referred to as mSLP). Notably, the mSLP platform exhibited increased adhesion and cellular

uptake by cancerous cells compared with uncoated lipid nanoparticles. Shortly after uptake, mSLP released active SN38 into the cytoplasm and was subsequently transported into the nucleus. In an experimental murine model of orthotopic 4T1 breast cancer, macrophage-mimetic mSLP not only effectively suppressed primary tumor growth but also reduced the overall burden of metastatic lesions in organs.

## 2. Materials and methods

### 2.1. Preparation of cell membrane-cloaked nanocamptothecin

Lipid nanoparticles loaded with the PCL<sub>28</sub>-SN38 conjugate were prepared using nanoprecipitation. Briefly, PCL<sub>28</sub>-SN38 was dissolved in acetone and a lipid mixture of egg phosphatidylcholine (Egg-PC), cholesterol, 1,2-Distearoyl-*sn*-glycero-3-phosphoethanolamine-N-[methoxy (polyethylene glycol) 2000] (DSPE-PEG<sub>2k</sub>) and dimethyldioctadecylammonium bromide (DDAB) was dissolved in ethanol at the mass ratio of 35:5:8:2. Next, the PCL<sub>28</sub>-SN38 conjugate and all the lipids were mixed in 1 mL of acetone with 60  $\mu$ L of ethanol and added dropwise to 2 mL of deionized (DI) water while stirring at room temperature. After 10 min of stirring, the remaining acetone was removed by a rotary evaporator at reduced pressure.

M1-type macrophages were obtained by stimulating RAW264.7 cells with 1  $\mu$ g/mL lipopolysaccharide (LPS) for 12 h. The cell membrane was isolated using the protocol previously reported by Pilchler et al. [28], and the bicinchoninic acid (BCA) protein assay was used to determine the protein content on the membrane. The isolated cell membrane from  $1 \times 10^8$  cells was mixed with 1 mL of polymeric SN38 lipid nanoparticles (SLP) at a concentration of 1 mg/mL of SN38. The mixture was then extruded through 400 nm polycarbonate membranes to prepare cell membrane-coated polymeric SN38 lipid nanoparticles (mSLP).

### 2.2. Characterization of nanoformulations

Particle sizes were characterized using dynamic light scattering (DLS). Using Malvern Nano-ZS90 instrument (Malvern, UK), hydrodynamic diameters ( $D_H$ ), size distribution and zeta potentials of the nanoparticles were determined at a 0.1 mg/mL SN38 equivalent concentration and at 25 °C. Morphology was characterized using transmission electron microscopy (TEM). SLP or mSLP with a 0.5 mg/mL SN38 equivalent concentration was dropped on a 300-mesh carbon-coated copper grid. After 2 min, the surface liquid was removed with filter papers, and the samples were stained with a 2 wt% aqueous uranyl acetate solution for 1 min. Morphological characterization was performed after the sample was air-dried using a TECNAI 10 microscope (Philips) at an acceleration voltage of 80 kV.

### 2.3. *In vitro* analysis of drug release kinetics

The drug release kinetics were quantified using the dialysis diffusion method. Three milliliters of nanocamptothecin solutions with a 0.1 mg/mL SN38 equivalent concentration (in PBS or 30 U/mL porcine liver esterase) were loaded into dialysis bags (Spectrum, molecular weight cutoff of 7 kD). Then end-sealed dialysis bags were placed in 20 mL of release medium (phosphate buffer solution, pH 7.4, with 0.4% Tween 80). Dialysis bags were continuously shaken at 100 rpm on an orbital shaker at 37 °C. The release medium containing the drugs was collected at predetermined time points, and the equal amount of release medium was added. Finally, the drug concentration was quantified using UV-Vis spectrometer (Shimadzu, UV-2700) at 378 nm.

### 2.4. Cell lines and cell culture

The cell lines were purchased from the cell bank of the Chinese Academy of Sciences (Shanghai, China). Cells were cultured with DMEM or RPMI-1640 supplemented with 10% fetal bovine serum (FBS), 100

units/mL penicillin and 100 µg/mL streptomycin at 37 °C with 5% CO<sub>2</sub> in a humid atmosphere.

### 2.5. *In vitro* cytotoxicity measured using the cell counting kit-8 (CCK-8) assay

A CCK-8 assay was employed to determine the *in vitro* cytotoxicity of CPT-11, free SN38, SLP and mSLP. Cells were seeded into 96-well plates at a density of 3000–5000 cells per well. After culture at 37 °C for 24 h, different concentrations of drugs were added to the cells. Then the cells were cultured for another 72 h. At the end of the exposure, CCK-8 solution was added proportionally to each well and incubated for approximately 1–2 h. The absorbance was determined at 450 nm using a microplate reader (Multiskan FC, Thermo Fisher Scientific).

For drug withdrawal, cells were preseeded as described above and treated with various drug concentrations. After incubations for 6 h, 12 h and 24 h, the drug-containing medium was replaced with fresh culture medium and incubated for 66 h, 60 h and 48 h, respectively. Finally, a CCK-8 assay was performed as described above.

### 2.6. Animal experiments

All animal studies were conducted in accordance with the National Institute Guide for the Care and Use of Laboratory Animals. The experimental protocols were approved by the Ethics Committee of the First Affiliated Hospital, Zhejiang University School of Medicine.

### 2.7. Analysis of the distribution *in vivo* using near-infrared (NIR) fluorescence imaging

We established an orthotopic 4T1 breast cancer model in BALB/c mice to investigate the tumor targeting capabilities of SLP and mSLP. DiR was encapsulated in SLP and mSLP and served as the probe of NIR fluorescence. When the tumor grew to 50–100 mm<sup>3</sup>, mice were randomized into two groups, and intravenously injected with DiR-loaded SLP and mSLP at an equivalent dose of DiR. Then the mice were anesthetized with isoflurane and the whole-body fluorescence images were acquired at 0.5 h, 2 h, 4 h, 8 h, and 24 h postadministration. At the 24 h time point, mice were sacrificed, and tumors and major organs were removed from each group and subjected to *ex vivo* imaging. Then, the dissected tumors were prepared as frozen sections, and stained with 4,6-diamidino-2-phenylindole (DAPI). The distribution of DiR-loaded SLP and mSLP was analyzed using fluorescence microscopy.

### 2.8. *In vivo* antitumor activity

The orthotopic 4T1 breast cancer model was established by injecting  $1 \times 10^6$  4T1 cells into the right fifth mammary gland fat pad of BALB/c mice. When the tumor volume reached approximately 50–100 mm<sup>3</sup>, the mice were randomly divided into 4 groups ( $n = 12$  mice per group). Mice in each group were injected with saline, CPT-11, SLP or mSLP at a 10 mg/kg SN38 equiv. dose through the tail vein. Mice were administered the drug on Days 0, 3 and 6. The body weight and tumor volume of the mice were measured every three days. The formula used to calculate the tumor volume was:  $V = (L \times W^2)/2$ , L: length, W: width, in which W was smaller than L. In addition, the tumors were dissected from each group and fixed with 4% formaldehyde. The tissue sections were subjected to hematoxylin and eosin (H&E, Sigma) staining. A Ki67 assay was performed to assess cell proliferation in tumor tissues. A terminal deoxynucleotidyl transferase-mediated dUTP-biotin nick end labeling (TUNEL) assay was utilized to evaluate cell apoptosis. The stained tumor sections were observed and photographed using a fluorescence microscope (IX71, Olympus).

For the assessment of spontaneous lung metastasis in the 4T1 orthotopic model, three of the mice described above were sacrificed on Day 24, and the main organs and the inguinal lymph nodes and axillary

lymph nodes on both sides in each mouse were dissected, photographed and weighed. The excised tumors and organs were then fixed with 4% formaldehyde and sectioned into 5-µm slices for H&E staining. The stained tumor slices were observed under a microscope (IX71, Olympus). Three visual fields of each slice were randomly selected for imaging and analysis.

### 2.9. Statistical analysis

All quantitative data are presented as the means ± standard deviations (SD). Statistical analyses were performed using Student's *t*-test. Statistical significance was indicated by *p* values < 0.05 (\*), <0.01 (\*\*), or <0.001 (\*\*\*)

## 3. Results and discussion

### 3.1. Packaging of cytotoxic lipid nanoparticles into the M1-type macrophage membrane

We previously showed that the anticancer agent SN38 reversibly ligated to a PCL fragment *via* a hydrolytic ester bond is stably assembled in a PEG<sub>10k</sub>-*b*-PCL<sub>10k</sub> polymer matrix [27]. Optimization of the PCL modifier through *in vitro* and *in vivo* investigation allowed us to identify that the PCL<sub>28</sub>-SN38 conjugate has the potential to substantially improve the therapeutic efficacy compared with its clinically approved counterpart CPT-11 (irinotecan). More importantly, we disclosed the structure-activity relationship for these cytotoxic nanoparticles. Here, we attempted to package a polymeric SN38 prodrug (i.e., PCL<sub>28</sub>-SN38 conjugate, <sup>1</sup>H NMR characterization is shown in Fig. S1) into a lipid formulation, followed by fusion of the M1-type macrophage membrane. The fabrication process of membrane-cloaked SN38 lipid nanoparticles (mSLP) is illustrated in Fig. 1. Prior to cell membrane collection, RAW264.7 macrophages were stimulated with 1 µg/mL LPS for 12 h to induce M1 polarization. After exposure to LPS stimulation, substantially increased levels of biomarkers related to M1-type macrophages were confirmed using real-time PCR (Fig. 2a). The cell membrane was then isolated and purified according to the protocol as described in the methods and blended with lipid nanoparticles. Finally, membrane cloaking on the surface of SLP was accomplished by extruding the mixture through polycarbonate membranes.

### 3.2. Characterization of membrane-cloaked nanocamptothecin

Transmission electron microscopy (TEM) visualization was conducted to observe the morphology. Both of the formulations exhibited spherical nanostructures, with sizes of ~80 and ~90 nm for SLP and mSLP in the solid-state (Fig. 2b and c). Compared with uncoated nanocamptothecin, a single cell membrane bilayer of ~10 nm was visible on the surface of mSLP. Measurement of hydrodynamic diameters ( $D_H$ ) using dynamic light scattering (DLS) revealed that the final mSLP was approximately 20 nm larger than bare SLP (Fig. 2d), with a polydispersity index (PDI) of less than 0.2 (Fig. 2e). Characterization of zeta potentials indicated a negatively charged surface (−22.8 mV), consistent with the surface charge of cell membranes (Fig. 2f). Representative photographs of both nanoparticle solutions are shown in Fig. S2, presenting homogeneous suspensions. In contrast, the parent SN38 agent were not miscible either with the lipid formulation or macrophage membrane components to form stable nanosuspensions (Fig. S3). We anticipated that membrane-associated protein content was translocated onto the artificial nanoparticles. Thus, the protein composition of mSLP was analyzed using sodium dodecyl sulfate–polyacrylamide gel electrophoresis (SDS–PAGE) to validate the biomarker profiles (Fig. 2g). M1-type macrophage membranes alone were included in parallel for comparison. Obviously, mSLP inherited a very similar proteinogram from macrophages, thereby enhancing adhesion to cancer cells. Integrin (α4, β1) and VCAM-1 are reported to

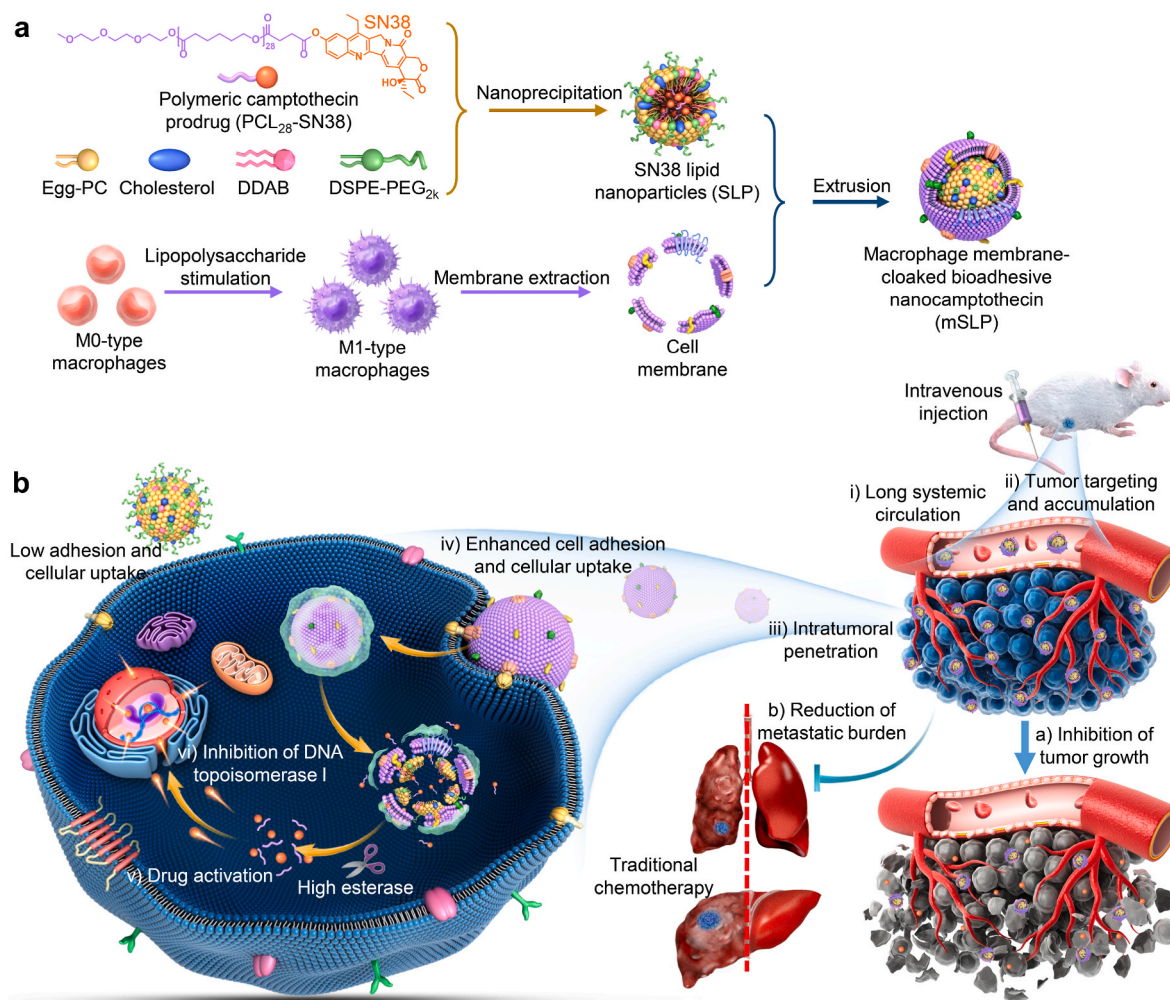


**Fig. 1.** (a) Schematic illustration of the procedure used to prepare macrophage membrane-camouflaged polymeric nanotherapy (mSLP). The esterase-activatable SN38 prodrug (PCL<sub>n</sub>-SN38,  $n = 28$ ) was synthesized and stabilized by lipid components. The SN38 lipid nanoparticles (SLP) were sequentially cloaked with LPS-stimulated M1-type macrophage membranes to increase cell adhesion and tumor cell uptake. (b) Following intravenous injection, mSLP had prolonged systemic circulation and preferentially accumulated at tumor sites. After uptake by cancer cells, mSLP effectively released the DNA topoisomerase I inhibitor SN38 in response to intracellular esterase to inhibit tumor growth and metastatic burden.

be involved in cell–cell interactions between macrophages and cancer cells [29,30]. We further examined the membrane proteins of mSLP using western blot analysis to identify these specific proteins (Fig. 2h). Using specific antibodies against  $\alpha 4$  and  $\beta 1$  integrin, the proteins were identified in both the cell membrane and mSLP, whereas no band was observed for SLP. These results confirmed that polymeric SN38 nanoparticles and membrane composition were assembled by physical fusion.

The stability of membrane-cloaked nanocamptothecin was further assessed when stored in different media using DLS analysis. Both nanoparticles remained adequately stable in PBS or PBS containing FBS (10%, v/v), with no observed variations in particle size and PDI over one week (Fig. 2i). Moreover, the nanoparticles did not precipitate during the observation. We further tested the stability of nanoparticles in PBS with mouse serum (10%, v/v) or FBS (90%, v/v). The results showed that mSLP were stable in these media but uncoated SLP was unstable and precipitated during the incubation in the solution with 90% FBS (Fig. S4). Sustained drug release kinetics from delivery vehicles after intravenous injection are particularly important and could promote improved pharmacokinetics and desirable intratumor accumulation [31]. We thus examined the mSLP release profile by dialyzing it against PBS release medium at 37 °C. In the absence of porcine liver esterase (PLE), mSLP showed a sustained rate of steady release, with no burst

release observed (Fig. 2j). Notably, accelerated liberation of SN38 occurred in the presence of PLE, showing a release rate of 71.5% after one-week of dialysis. The major released species is active SN38 agent as determined by HPLC analysis (Fig. S5). This esterase-activatable and sustained release pattern is consistent with our previously reported result. Although slow drug release may potentially compromise cytotoxicity *in vitro*, animal studies have shown that slow release contributes to higher stability and greater tumor accumulation and drug efficacy *in vivo*.

### 3.3. *In vitro* cytotoxicity profiles of membrane-camouflaged nanoparticles

Cytotoxic potency against cancer cells *in vitro* is an important indicator of *in vivo* therapeutic efficacy. We therefore assessed the potency of membrane-camouflaged camptothecin nanotherapy mSLP against melanoma B16F10 and breast 4T1 cancer cell lines by performing a cell counting kit-8 (CCK-8) assay. In this assay, free SN38 and its water-soluble prodrug CPT-11 were included as controls. The half maximal inhibitory concentration (IC<sub>50</sub>) of each drug was extrapolated from the dose–response curve and are shown in Fig. 3a and b. In both cell lines, the IC<sub>50</sub> values of both formulations were a nanomolar concentration that was approximately two orders of magnitude higher than the potency of the clinically approved drug CPT-11. These data implied that

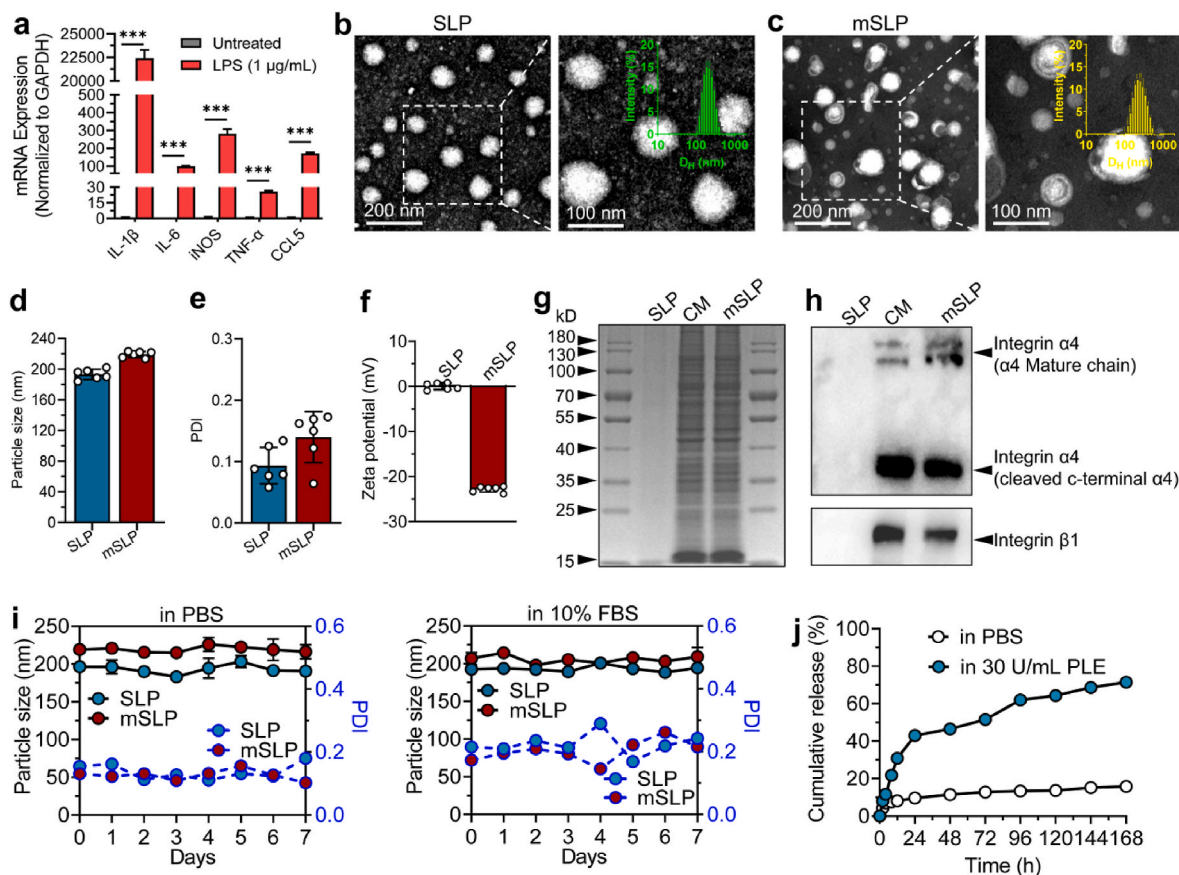


**Fig. 2.** Preparation and characterization of macrophage membrane-camouflaged nanocamptothecin. (a) Real-time PCR analysis of the mRNA expression of M1-type macrophage markers. Transmission electron microscopy images of (b) uncoated lipid nanoparticle SLP and (c) membrane-cloaked mSLP. Insets show the size distribution of nanoparticles measured using dynamic light scattering (DLS). (d) Hydrodynamic diameter ( $D_h$ ), (e) polydispersity index (PDI), and (f) zeta potential of nanoparticles. (g) Protein profiles of SLP, M1-type macrophage cell membrane (CM) and mSLP analyzed using SDS–PAGE. (h) Expression of integrin  $\alpha 4$  and integrin  $\beta 1$  in each sample measured using western blotting. (i) Stability assessed by measuring changes in the size and PDI in phosphate-buffered saline (PBS) or in PBS containing 10% (v/v) FBS at 37 °C. (j) *In vitro* drug release profiles in PBS (pH = 7.4) and PBS containing 30 U/mL porcine liver esterase (PLE). Data are presented as the means  $\pm$  SD.

the CPT-11 prodrug was insufficiently converted into the active drug form. Unexpectedly, compared with free SN38, no significant reduction in the *in vitro* cytotoxicity was observed for covalently conjugated prodrug formulations. In general, covalently ligated prodrugs require the bond cleavage to regain their activities, which will reduce drug activity *in vitro*. However, the results presented here indicate that M1-type macrophage membrane-cloaked nanotherapy was effectively endocytosed by cells and intracellularly released active SN38 to kill tumor cells.

We designed an additional cell-based cytotoxicity analysis to further verify whether surface cloaking of the macrophage membrane impacts drug activity (Fig. 3c). After cells were exposed to the treatment for different times (e.g., 6, 12 or 24 h), the cell culture media with the drugs were replaced with fresh culture media. Following additional culture, cell viability was analyzed using the CCK-8 assay (Fig. 3c). Compared with SLP, mSLP exerted superior inhibitory effects on both B16F10 and 4T1 cancer cells (Fig. 3d and e). Taken together, these *in vitro* data indicate that the polymer prodrug overcomes the low enzymatic conversion rate of the clinically approved drug CPT-11. Furthermore, exploiting macrophage membrane cloaking, the platform effectively delivered more therapeutic agents into cancer cells and produced higher potency.

### 3.4. Mode-of-action of membrane-camouflaged nanotherapy on cancer cells

We performed an Annexin V/propidium iodide (PI) dual staining

assay to investigate whether nanoparticle-induced cell death was mediated by apoptosis. FITC-conjugated Annexin V binds to translocated phosphatidylserine of apoptotic and necrotic cells, whereas PI is a nucleic acid dye of late apoptotic and necrotic cells, thus discriminating between apoptosis and necrosis [32]. SN38-loaded bare nanoparticle SLP and membrane-cloaked nanoparticle mSLP exhibited a comparable potency to induce cell apoptosis compared with free SN38 in the two tested cell lines (Fig. 4a and b). The apoptotic rates for mSLP were high as  $50.1 \pm 1.5\%$  and  $46.1 \pm 0.7\%$  in B16F10 and 4T1 cells, respectively, after 48 h of treatment. Cellular DNA synthesis was detected using an EdU (5-ethynyl-2'-deoxyuridine) incorporation assay to clarify the antiproliferative activity of mSLP. Compared with the untreated cells, the number of EdU-positive proliferating cells decreased significantly after nanoparticle treatment in both B16F10 (Fig. 4c and d) and 4T1 (Fig. 4e and f) cells. Notably, mSLP exerted a greater inhibitory effect than SLP, indicating a stronger antiproliferative capability of mSLP. Taken together, mSLP exhibited superior antitumor activity *in vitro*.

SN38 is the active metabolite of CPT-11, a potent DNA topoisomerase I inhibitor, which can lead to DNA damage during replication or transcription and result in cell cycle arrest at the G2/M phase [33,34]. We probed the effect of free SN38 and nanoparticles on the cell cycle progression. By performing cell cycle analysis, we found that treatment of both SLP and mSLP significantly increased the proportion of G2/M phase cells and decreased the proportion of G1 phase cells, thus arresting the cell cycle at the G2/M phase (Fig. 4g and h). These data

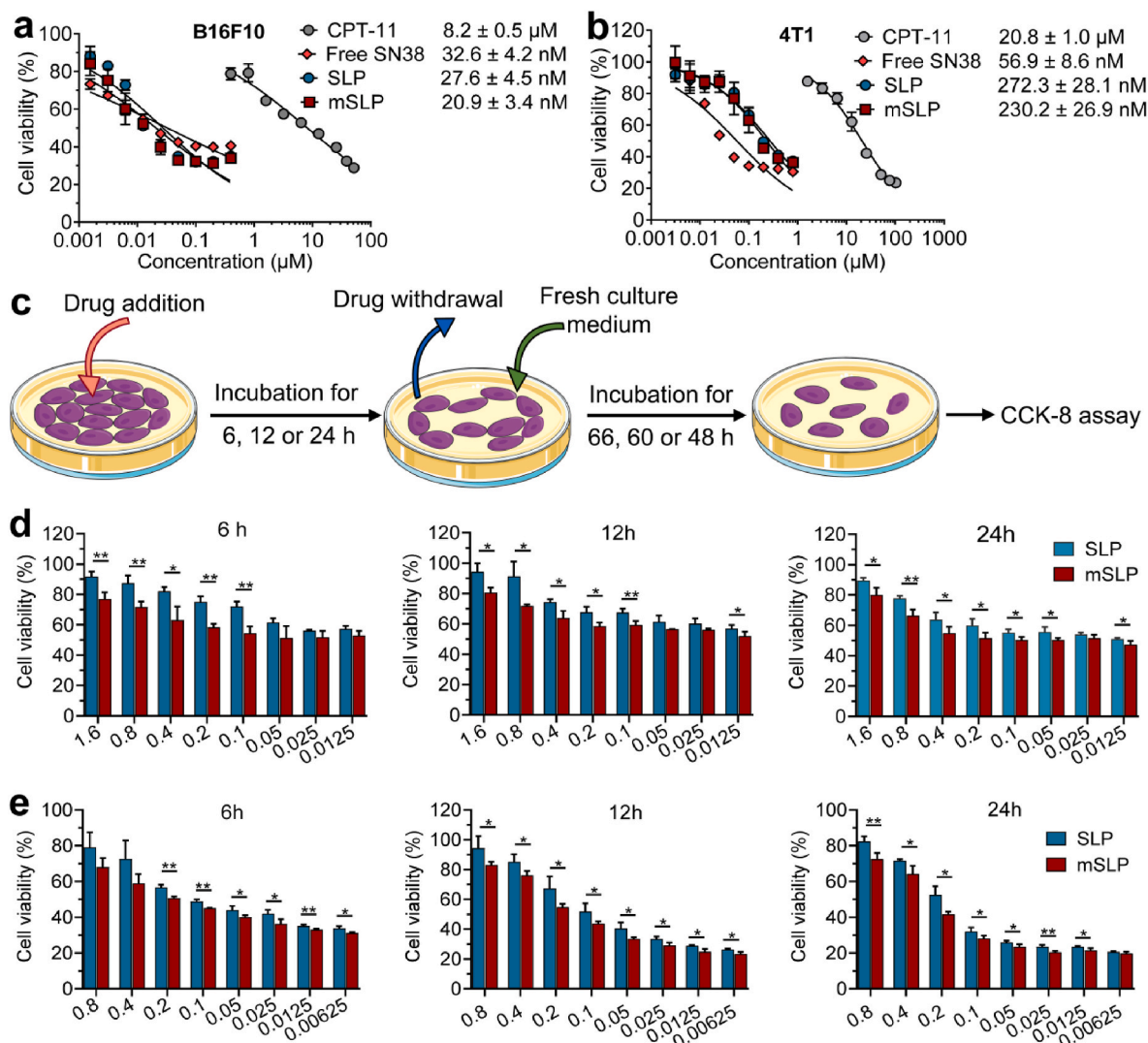


**Fig. 3.** *In vitro* cytotoxicity of nanocamptothecin. The cytotoxicity of CPT-11, free SN38, SLP and mSLP toward (a) B16F10 and (b) 4T1 cancer cells, as determined using the CCK-8 assay. IC<sub>50</sub> values were calculated based on the dose–response curves. (c) A schematic diagram illustrating the experimental protocol for drug withdrawal. Viability of (d) B16F10 and (e) 4T1 cancer cells after an incubation with drugs for 6 h, 12 h and 24 h, and subsequent incubation with fresh medium. Data are presented as the means ± SD. \**p* < 0.05, and \*\**p* < 0.01.

suggested that SN38-loaded nanoparticles indeed induced remarkable cell cycle arrest, which is consistent with the previous cytotoxicity results.

### 3.5. Macrophage membrane cloaking enhances nanoparticle adhesion to cancer cells and increases cellular uptake

The endocytosis of therapeutic nanoparticles requires two steps: nanoparticles adhere to the cell membrane, followed by active internalization into the cells [35]. We first evaluated the adhesive potential of the two nanoparticles. All nanoparticles were labeled with DiI dye and incubated with 4T1 and B16F10 cells at 4 °C for 4 h to facilitate the analysis (Fig. 5a). Concurrently, the cell membrane was labeled with green lectin and the nuclei were stained with Hoechst. The results derived from confocal laser scanning microscopy (CLSM) revealed that the retention of SLP on both cell monolayers was negligible. In contrast, mSLP exhibited much higher cell adhesion and exhibited colocalization with green lectin. Thus, macrophage membrane cloaking ensured the avid bioadhesion of nanoparticles to cancer cell surfaces, probably due to the intrinsic protein–protein interaction between the membranes of macrophages and cancer cells.

Intrigued by the increased adhesion of mSLP on cancer cells, we then evaluated the cellular uptake of SLP and mSLP in cancer cells. After an incubation of DiI-labeled nanoparticles with 4T1 or B16F10 cells at 37 °C for 4 h, the intracellular fluorescence intensity was quantified using flow cytometry. Compared with bare SLP, we detected a notably higher frequency of DiI-positive cells and increased fluorescence intensities in mSLP-treated 4T1 (Fig. 5b) and B16F10 (Fig. 5c) cells. We tracked the intracellular distribution of nanoparticles using CLSM to further elucidate the uptake pathway. 4T1 cells were exposed to the two DiI-labeled nanoparticles, and the endo/lysosomal compartment was marked with LysoTracker Green. Again, red fluorescence signals from SLP-treated cells were negligibly observed in CLSM images (Fig. S6). On the other hand, the time-lapse fluorescence images showed that most mSLP was trafficked to endo/lysosomes, as evidenced by good colocalization with LysoTracker Green at the early time points (Fig. 5d). Subsequently, red signals increased over time and were not colocalized with endo/lysosomes at 20 h, suggesting that mSLP could escape into the cytosol.

According to previous studies, nanoparticles are internalized into cells through multiple endocytosis pathways [36,37]. Cells were pre-treated with several endocytosis inhibitors for this experiment to clarify

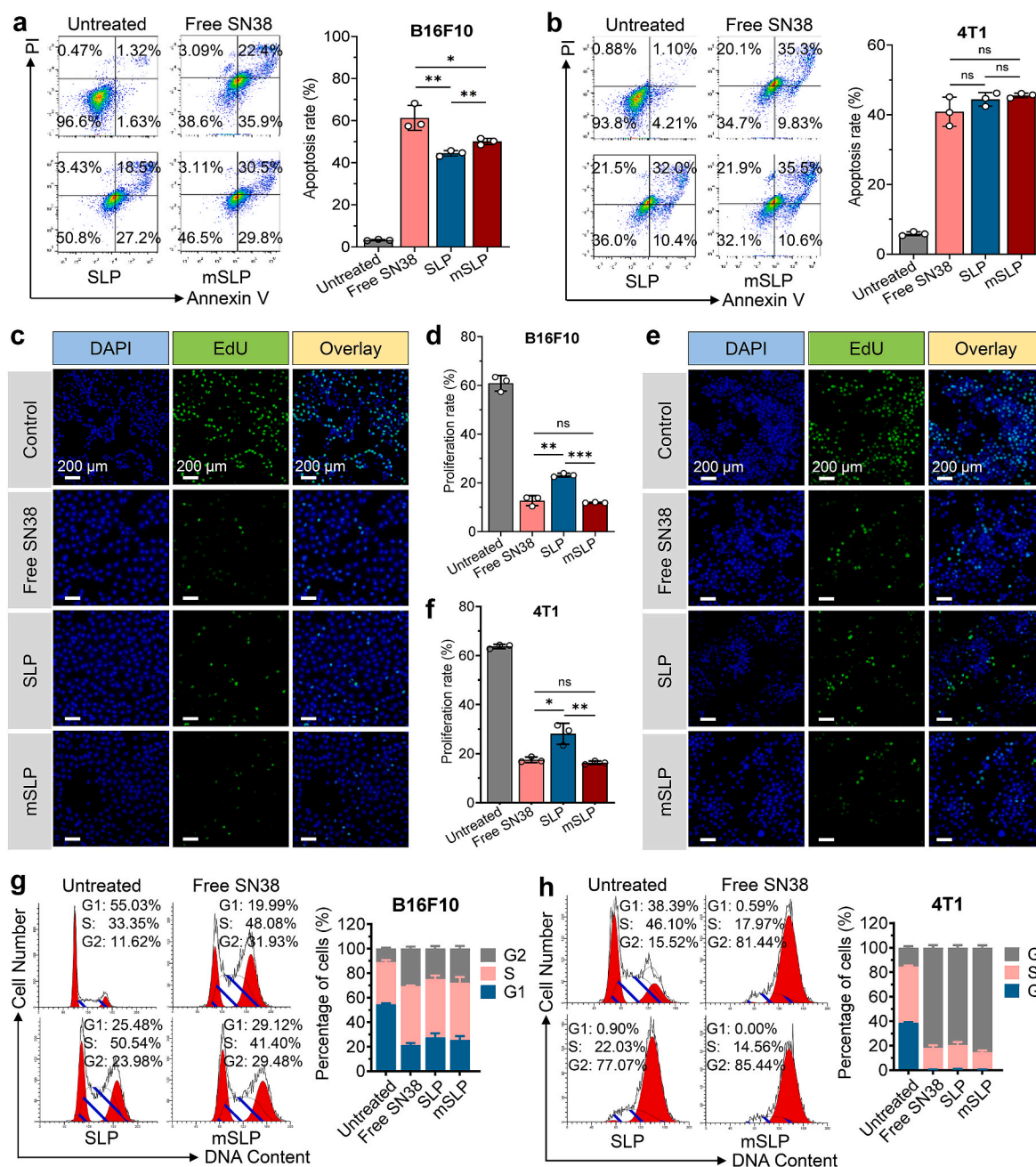


**Fig. 4.** Cell apoptosis, proliferation inhibition, and cell cycle arrest induced by nanocamptothecin. Apoptosis of (a) B16F10 and (b) 4T1 cells after drug treatment was detected by staining with FITC Annexin V/PI and flow cytometry analysis ( $n = 3$ ). Proliferation of (c and d) B16F10 and (e and f) 4T1 cells after exposure to drugs, as determined by the Click-iT EdU assay ( $n = 3$ ). Cell cycle distribution of B16F10 (g) and 4T1 (h) cells after exposure to drugs, as determined by flow cytometric analysis ( $n = 3$ ). Data are presented as the means  $\pm$  SD. \* $p < 0.05$ , \*\* $p < 0.01$ , and \*\*\* $p < 0.001$ .

the uptake pathways of this membrane-cloaked nanoparticle system. Chlorpromazine (CPZ) is a known cationic amphiphilic inhibitor of clathrin-dependent endocytosis, cytochalasin D (CytD) is an inhibitor of macropinocytosis, and filipin III blocks caveolin-mediated endocytosis. After pretreatment using inhibitors, 4T1 cells were incubated with fluorescent mSLP and analyzed with flow cytometry (Fig. 5e and f). Compared with the untreated cells, pretreatment with CPZ resulted in a remarkable decrease in the cellular uptake of mSLP, whereas no significant reduction in nanoparticle uptake was observed after either CytD or filipin III treatment. We thus concluded that clathrin-mediated endocytosis was the principle mechanism of membrane-cloaked nanoparticle uptake by tumor cells.

### 3.6. M1-type macrophage membrane cloaking increases the intratumor delivery of nanotherapy

We conducted the pharmacokinetic (PK) study to verify whether macrophage membrane cloaking could render the nanoparticles with the prolonged systemic circulation. After a single intravenous injection of different formulations to Sprague-Dawley (SD) rats, blood samples were collected at the predetermined time and subjected to HPLC analysis. Plasma concentration-time curves and PK parameters determined by non-compartmental analysis are summarized in Fig. 6a and Table 1, respectively. Compared with the rapid clearance of the clinically approved drug CPT-11 ( $t_{1/2}$ :  $0.63 \pm 0.05$  h), nanocamptothecin exhibited longer circulation time in the blood ( $t_{1/2}$ :  $17.41 \pm 1.47$  h and  $20.15$

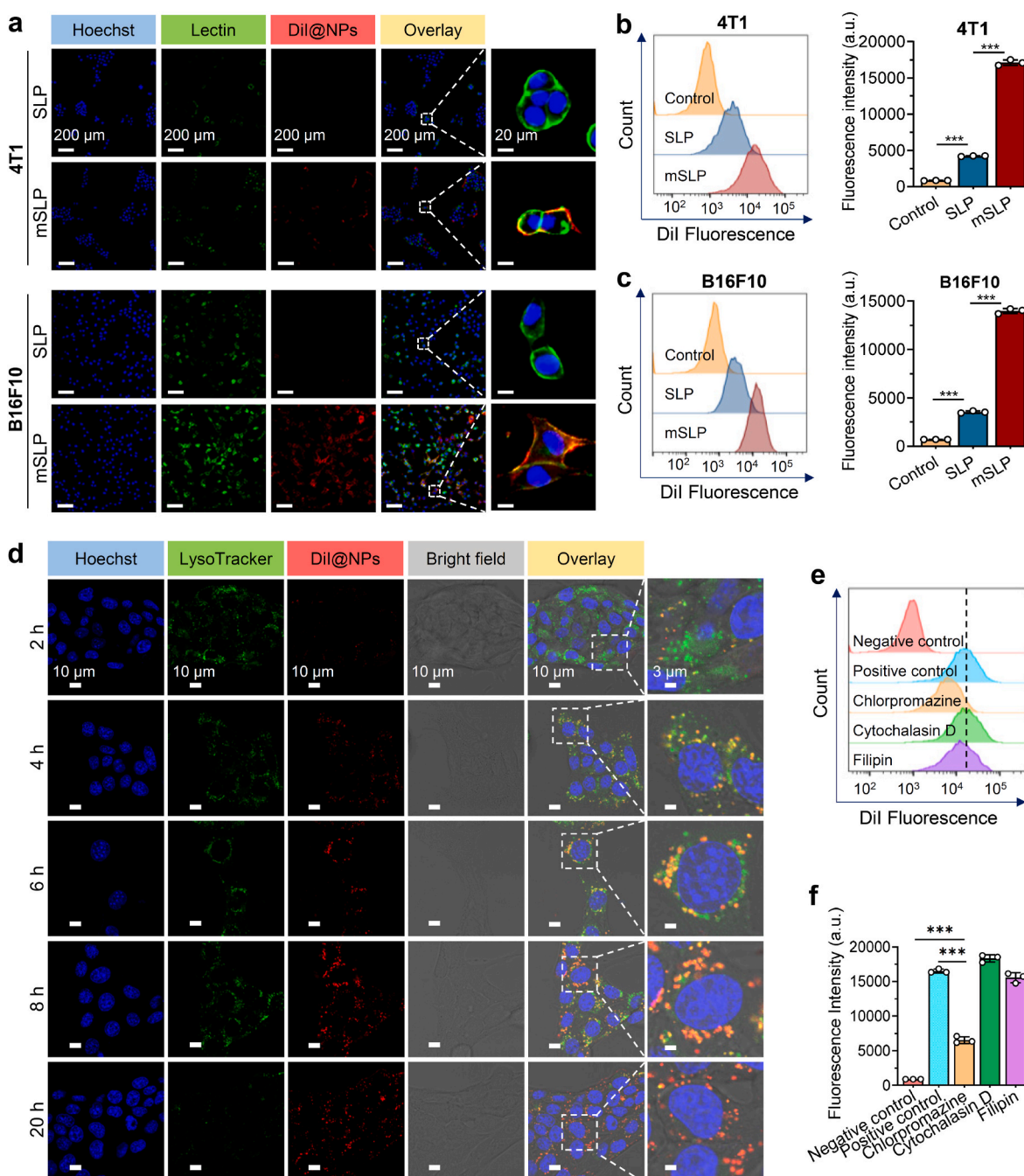


**Fig. 5.** Adhesion and cellular uptake of macrophage membrane-cloaked nanocamptothecin. (a) Nanoparticle adhesion to 4T1 and B16F10 cells was examined using confocal laser scanning microscopy (CLSM). The cell membrane was labeled with lectin (green), and cell nuclei were stained with Hoechst (blue). Flow cytometry analysis of DiI-labeled nanoparticle cellular uptake after 4 h of incubation at 37 °C in (b) 4T1 and (c) B16F10 cells ( $n = 3$ ). (d) Intracellular distribution of DiI-labeled mSLP observed with time-lapse confocal microscopy. Endo/lysosomes were stained with LysoTracker (green), and cell nuclei were stained with Hoechst (blue). (e and f) Uptake pathway of mSLP analyzed using flow cytometry. Cells were pretreated with various inhibitors of different endocytosis pathways ( $n = 3$ ). Data are presented as the means  $\pm$  SD. \*\*\* $p < 0.001$ .

$\pm 0.42$  h for SLP and mSLP, respectively). The data derived from the area under the concentration-time curve (AUC) further supported the improved PK property. For example,  $AUC_{0-t}$  of mSLP was 2.0-fold greater than that of SLP ( $388.71 \pm 5.54 \mu\text{g h/mL}$ ), which was further 321-fold greater than that of CPT-11 ( $2.39 \pm 0.41 \mu\text{g h/mL}$ ). Therefore, the combinatorial strategy that uses polymeric prodrug design and cell membrane cloaking endows the nanotherapeutics with improved PK property, resulting from the high stability and steady drug release kinetics.

Inspired by the increased intracellular uptake and improved circulation, we further investigated whether M1-type macrophage membrane-camouflaged nanoparticles have the tropism toward tumor lesions. For this purpose, the NIR dye DiR was used to label the nanoparticles. We measured the *in vivo* biodistribution of the nanoparticles in an orthotopic 4T1 breast cancer model that was established in immunocompetent BALB/c mice. Following a single injection of DiR-labeled nanoparticles into the tail vein, the whole-body fluorescence imaging of mice was performed using IVIS imaging, which enables a comparison of the *in vivo* retention of NIR dye-labeled nanotherapies. As shown in

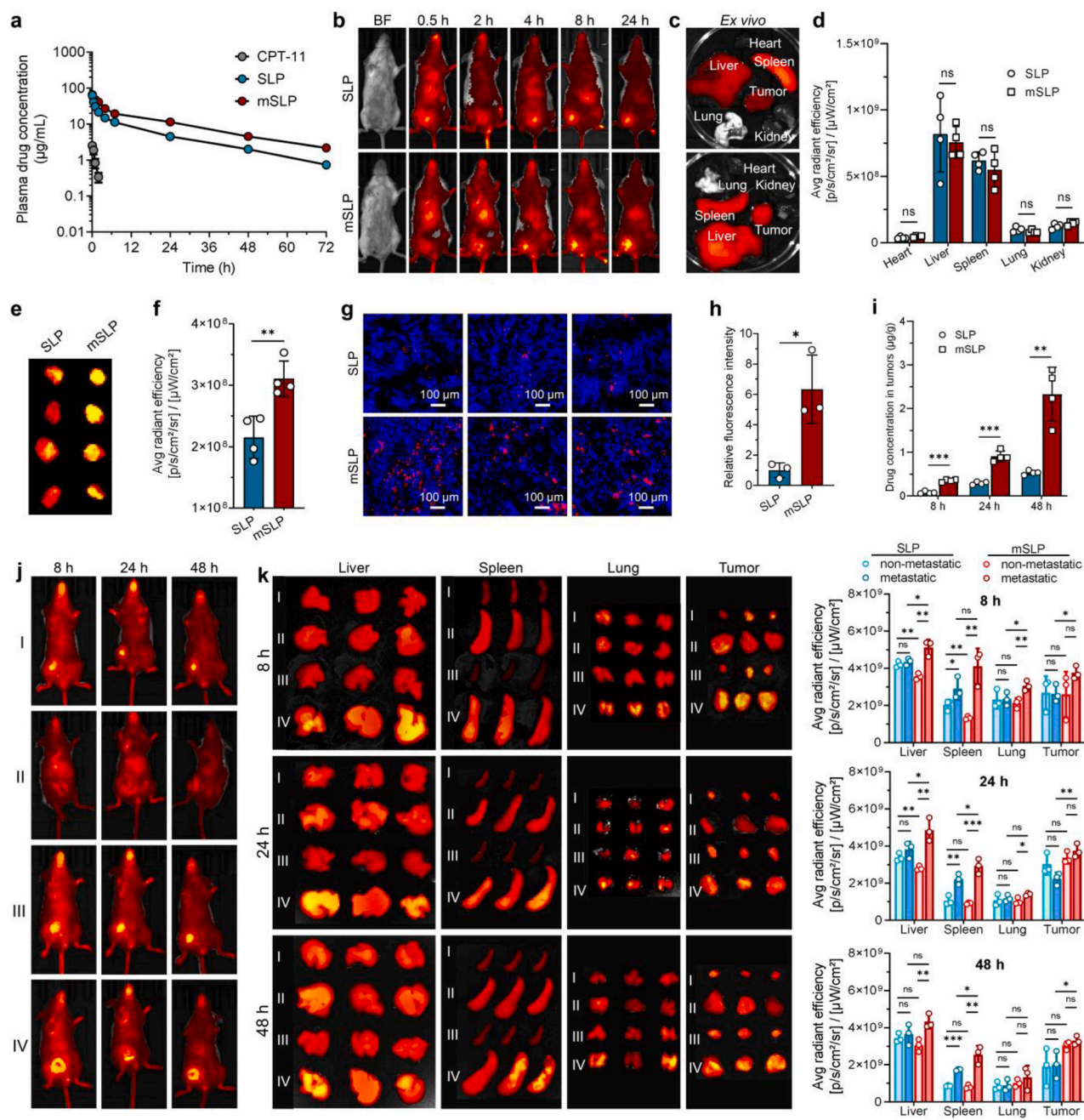


**Fig. 6.** Pharmacokinetic study and *in vivo* tumor targeting capacity of nanoparticles. (a) Plasma SN38 concentration-time profiles in SD rats after a single intravenous injection of CPT-11, SLP or mSLP via the tail vein. The drug dose was 10 mg/kg (SN38 equiv.). (b) Real-time *in vivo* NIR fluorescence images of mice bearing orthotopic 4T1 breast tumors after an intravenous injection of DiR-labeled nanoparticles. (c) *Ex vivo* fluorescence images of excised tumors and major organs (heart, liver, spleen, lung and kidneys) captured at 24 h post injection. BF: bright field. (d) Quantitative analysis of the average radiant efficiency in major organs ( $n = 4$ ). (e and f) Images and average radiant efficiency of tumors from SLP- and mSLP-treated mice ( $n = 4$ ). (g and h) Fluorescence images and intensities of tumor tissue sections visualized using fluorescence microscopy ( $n = 3$ ). (i) Drug concentrations in the mouse model of orthotopic 4T1 breast cancer after a single injection of nanotherapeutics at 15 mg/kg SN38 equiv. dose. Drug concentrations were determined by HPLC analysis at 8, 24, and 48 h postadministration. (j) Real-time *in vivo* NIR fluorescence images of mice after intravenous injection of DiR-labeled nanoparticles. (I) SLP, in the non-metastatic mouse model; (II) SLP, in the spontaneous metastatic mouse model; (III) mSLP, in the non-metastatic mouse model; (IV) mSLP, in the spontaneous metastatic mouse model. (k) *Ex vivo* fluorescence images of major organs (liver, spleen and lung) and excised tumors, and quantitative analysis of fluorescence intensities obtained at 8 h, 24 h and 48 h post injection ( $n = 3$ ). Data are presented as the means  $\pm$  SD. \* $p < 0.05$ , \*\* $p < 0.01$  and \*\*\* $p < 0.001$ .

Fig. 6b, fluorescent signals derived from DiR showed sustained retention in both nanotherapeutic-treated mice and did not decrease substantially during a 24-h observation period. Notably, the mice injected with membrane-camouflaged mSLP presented bright NIR fluorescence signals in the tumor region, and the signals increased over time. We also measured the biodistribution of the two types of nanoparticles 24 h post

injection. The mice were sacrificed, and major organs and tumors were subjected to *ex vivo* imaging (Fig. 6c–f). Quantitative data revealed higher fluorescence intensities in tumors from the mSLP group than those in the SLP group, indicating that cloaking with the macrophage membrane endows the nanotherapeutics with a better tumor targeting capability (Fig. 6e and f). For both nanotherapeutics, predominant

**Table 1**

Pharmacokinetic parameters of CPT-11 (15 mg/kg), SLP, and mSLP (10 mg/kg SN38 equiv.).

PK parameter	Drug formulations		
	CPT-11	SLP	mSLP
$t_{1/2}$ (h)	0.63 ± 0.05	17.41 ± 1.47	20.15 ± 0.42
AUC <sub>(0-t)</sub> (μg·h/mL)	2.39 ± 0.41	388.71 ± 5.54	767.28 ± 13.15
AUC <sub>(0-inf)</sub> (μg·h/mL)	2.70 ± 0.53	407.17 ± 5.11	829.73 ± 12.39
CL (mL/h)	762.57 ± 144.65	4.91 ± 0.06	2.41 ± 0.04
Vd (mL)	684.31 ± 92.70	123.37 ± 10.2	70.1 ± 2.45
MRT (h)	0.86 ± 0.08	19.52 ± 0.64	25 ± 0.22
C <sub>max</sub> (μg/mL)	2.50 ± 0.27	62.47 ± 3.28	65.17 ± 1.88
C <sub>0</sub> (μg/mL)	2.65 ± 0.24	68.12 ± 4.25	68.27 ± 2.31

$t_{1/2}$ , elimination half-life; AUC, area under the curve of a plasma concentration versus time profile; AUC<sub>(0-t)</sub>, AUC from 0 to time t; AUC<sub>(0-inf)</sub>, AUC extrapolated to infinity; CL, total plasma clearance following intravascular administration; Vd, volume of distribution; MRT, mean residence time; C, drug concentration. Data are presented as the means ± SD (n = 5).

accumulation in the liver and spleen was also observed (Fig. 6c and d), and no statistically significant differences in fluorescence intensities in these organs were observed between the SLP and mSLP treatment groups (Fig. 6d). Cryosections obtained from dissected tumors of each group were imaged using CLSM to confirm whether mSLP penetrated and accumulated in the tumor (Fig. 6g-h). The intratumor NIR signals of mSLP were much stronger than those of SLP, and more interestingly, mSLP penetrated throughout the tumor tissues. Furthermore, we measured SN38 concentrations in tumors after dosing SLP or mSLP (Fig. 6i). Treatment of mSLP resulted in higher intratumor drug concentrations than SLP at each time point. Hence, consistent with the *in vitro* CLSM results, these *in vivo* results showed that M1-type macrophage membrane decoration facilitated the intratumor delivery and penetration of cytotoxic nanotherapy.

We further investigated the targeting capacity of membrane-cloaked nanocamptothecin in the metastatic model. Tumorigenesis and spontaneous metastasis to liver, spleen and lung occurred on day 35 after orthotopic inoculation of 4T1 breast cells into mice. In addition, a non-metastatic tumor model established at an early time point (e.g., day 7) after orthotopic injection of 4T1 cells was included in this experimental setting. As illustrated in Fig. 6j, both nanoparticles showed good penetration into small primary tumors at all time points. Intriguingly, mSLP exhibited higher accumulation in large primary tumors than SLP. At different time points postadministration, the major organs and tumors were dissected, and *ex vivo* NIR fluorescence imaging was performed (Fig. 6k). Quantitative data indicated that mSLP had the ability to preferentially accumulate in the liver, spleen and lung with metastatic foci as compared with SLP (Fig. 6k). No statistically significant differences were observed in fluorescence intensities in major organs between the non-metastatic and metastatic mouse models after injection of SLP. Interestingly, in the mice receiving mSLP treatment, we observed higher fluorescent signals in the organs with metastases relative to non-metastatic organs (Fig. 6k). Quantitative drug concentrations analyzed by HPLC also verified the above results (Fig. S7). Collectively, these data indicated that membrane camouflage could facilitate drug accumulation at the orthotopic tumor and metastatic foci and endowed nanocamptothecin with better tumor-targeting capacity.

### 3.7. *In vivo* antitumor activity against orthotopic breast cancer

Triple-negative breast cancer (TNBC), a subtype (~16%) of breast tumors defined by a lack of estrogen receptor, progesterone receptor and HER2 (also called ERBB2 or NEU), is a clinically aggressive and invasive cancer [38]. However, treatment options for TNBC remain limited. Inspired by the superior cytotoxic activity and preferential intratumor delivery, we evaluated the efficacy of M1 macrophage membrane-camouflaged nanotherapy in a preclinical TNBC mouse

model. Implantation of mouse 4T1 cancer cells into the right fifth mammary gland fat pad enabled us to establish an orthotopic breast cancer model in BALB/c mice. When the tumor volume grew to ~100 mm<sup>3</sup>, mice were divided randomly into four groups (n = 9 mice per group) and treated with saline, CPT-11, SLP, or mSLP (at a 10 mg/kg SN38 equiv. dose) on days 0, 3, and 6. As shown in Fig. 7a, the group receiving CPT-11 treatment presented a similarly rapid tumor growth compared with the saline-treated group, suggesting that the clinically approved drug was not sufficient to attenuate this aggressive disease. Encouragingly, the administration of both nanotherapies resulted in substantial suppression of the primary tumor growth. Notably, mSLP exhibited superior activity, inhibiting progression of the tumors compared with SLP ( $p < 0.001$ ). The mSLP treatment group also presented a significantly improved survival rate (Fig. 7b). In addition, the body weight change in each treatment group was monitored, and the stable body weight reflected the safety of dosing animals with these nanoparticles (Fig. 7c).

A histopathological analysis was performed to further explore the therapeutic potential (Fig. 7d). The tumor tissues from each group were sectioned and subjected to H&E staining to observe cell morphology. Tumor cells were profoundly destroyed after exposure to the nanotherapies. For example, a large number of tumor cells with pyknotic nuclei and vacuolated cytoplasm were extensively detected, suggesting cytotoxic SN38-induced intratumor apoptosis and necrosis. In contrast, tumor tissues from the saline- and CPT-11-treated groups displayed characteristics of tightly arranged tumor cells with large nuclei and cytologic atypia. Ki67 and TUNEL staining were subsequently performed to evaluate the capacities of different treatments to inhibit proliferation and induce apoptosis of tumor cells, respectively. Ki67 is a well-established biomarker for cancer cell proliferation, and a decreased Ki67% indicates a better antitumor profile for drug candidates [39,40]. In the nanoparticle-treated groups, intratumor expression of Ki67 was substantially decreased, especially in the mSLP group. Furthermore, TUNEL is a sensitive index for apoptotic cancer cells. Treatment with mSLP nanoparticles resulted in a remarkably higher level of intratumor apoptosis. Consistent with the tumor growth curves, the histological analysis also confirmed that the covalent formulation of cytotoxic SN38 into M1-type macrophage membrane-cloaked nanoparticles was an effective approach to enhance the antitumor efficacy.

The antitumor potential of biomimetic nanocamptothecin was further evaluated in another orthotopic TNBC mouse model using Py8119 cells, a mesenchymal-like murine mammary tumor cell line. The cells were injected into the fifth mammary gland fat pad of C57/BL6 mouse to establish the tumor model. After injection of DiR-labeled nanoparticles, mSLP treatment resulted in a stronger NIR fluorescence in tumor sections than SLP, and mSLP infiltrated throughout the tumor tissues (Fig. S8). A similar trend of tumor inhibition was observed in this model. Membrane-cloaked nanocamptothecin showed a significantly higher tumor inhibition activity than SLP and CPT-11 (Fig. 7e) and had little toxicity, evident by stable growth of body weights (Fig. 7f). The therapeutic superiority of mSLP also was supported by the tumors and tumor weights analyzed at the endpoint of the study (Fig. 7g and h). We also performed histopathological analysis of tumor tissues using H&E, Ki67 and TUNEL staining to validate the treatment efficacy (Fig. 7i).

### 3.8. *In vivo* antimetastatic activity in a 4T1 spontaneous metastasis model

TNBC is an aggressive form of breast cancer with high rates of recurrence and metastasis. As shown in previous studies, inoculated 4T1 tumor xenografts will metastasize to multiple organs including the liver, lung and lymph nodes [41]. As a method to extend the translational significance of this membrane-camouflaged platform, we examined the ability of nanocamptothecin to treat metastasis of murine TNBC xenografts. Seven days after the orthotopic inoculation of 4T1 cells, mice were intravenously injected with mSLP three times. On Day 24 after administration, mice were sacrificed and the major organs (heart, liver,

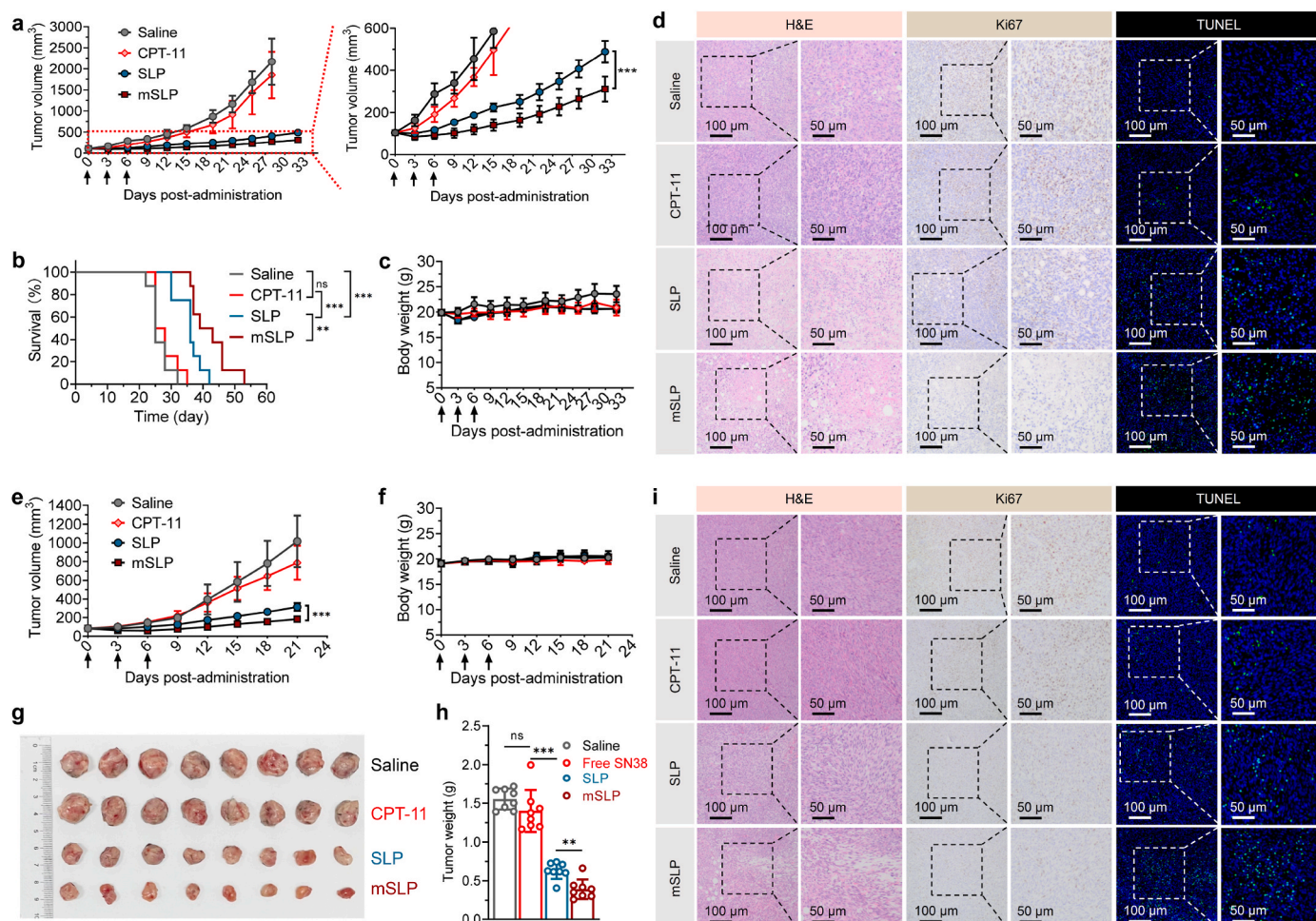


**Fig. 7.** *In vivo* antitumor activity of nanoparticles in preclinical TNBC mouse models bearing 4T1 tumors (a–d) and Py8119 tumors (e–i). (a) Tumor progression curves in the 4T1 orthotopic tumor-bearing mouse model after different drug treatments ( $n = 8$ ). (b) Survival curves of mice from different treatment groups ( $n = 8$ ). (c) Body weight changes monitored in mice from each group ( $n = 8$ ). (d) H&E, Ki67 and TUNEL staining of tumor sections. (e) Tumor progression curves in the Py8119 orthotopic tumor-bearing mouse model after different drug treatments ( $n = 8$ ). (f) Body weight changes monitored in mice from each group ( $n = 8$ ). (g and h) Photograph and weights of excised tumors in each group at the endpoint of the study. (i) H&E, Ki67 and TUNEL staining of tumor sections. Data are presented as the means  $\pm$  SD. \*\* $p < 0.01$ , and \*\*\* $p < 0.001$ .

spleen, lung and kidneys) and lymph nodes (inguinal lymph nodes and axillary lymph nodes) were dissected and macroscopically observed (Fig. 8a). Cancer cells, including TNBC, commonly migrate regionally to the lymphatic system before forming distant metastases. Therefore, we first compared the weight of lymph nodes dissected from the drug-treated mice. Quantitative analysis of the tissue weight revealed that lymph nodes from the mice receiving nanotherapy treatment were substantially smaller than those of mice receiving saline or CPT-11 treatment (Fig. 8b). In particular, the right inguinal lymph node of the mSLP group was smaller than that of the SLP group, implying a decreased metastatic tumor burden in the tumor-draining lymph node (dLN) following mSLP treatment. We further histologically analyzed ipsilateral inguinal lymph with H&E staining and did not observe metastatic foci in lymph nodes after administrating nanotherapies (Fig. 8c). In sharp contrast, CPT-11 treatment did not significantly reduce the metastatic burden of 4T1 cancer cells in the lymph compared to saline treatment.

No differences in the weights of other organs were observed (Fig. S9). However, we clearly detected metastasizing tumor cells in liver and lung after either CPT-11 or SLP treatment (Fig. 8d). Encouragingly, the administration of mSLP only resulted in a limited number of 4T1 tumor cells that were constrained in liver vessels but absent in the lung, suggesting that mSLP was sufficiently capable of inhibiting the metastatic

lesions. 4T1 tumor-bearing mice tend to develop splenomegaly. Interestingly, significant decreases in spleen size and weight were observed following the administration of nanoparticles. A histological analysis of spleens from the mice also confirmed this effect (Fig. 8e and f). Collectively, these results substantiated that our prodrug nanoplatform minimized tumor cell colonization to lymph nodes and other main organs, thus alleviating the metastatic burden. In addition, membrane-camouflaged mSLP exerted a better antimetastatic effect than SLP, possibly due to the superior *in vivo* tumor targeting capacity and ready endocytosis by tumor cells.

#### 4. Discussion

Pharmaceutical delivery of active compounds by synthetic nanocarriers provides several advantages over free drug delivery. Therapeutic agents are stabilized in nanoparticle matrices during blood circulation while being released and activated at targeted tumor lesions. Surface cloaking with hydrophilic materials renders nanotherapies stealthy for prolonged systemic circulation, which might increase the delivery of the therapeutic agent to disease sites. For example, PEGylation avoids immunological recognition and improves the pharmacokinetic properties of nanotherapies [7]; however, repeated administration of PEGylated nanoparticles is reported to accelerate the

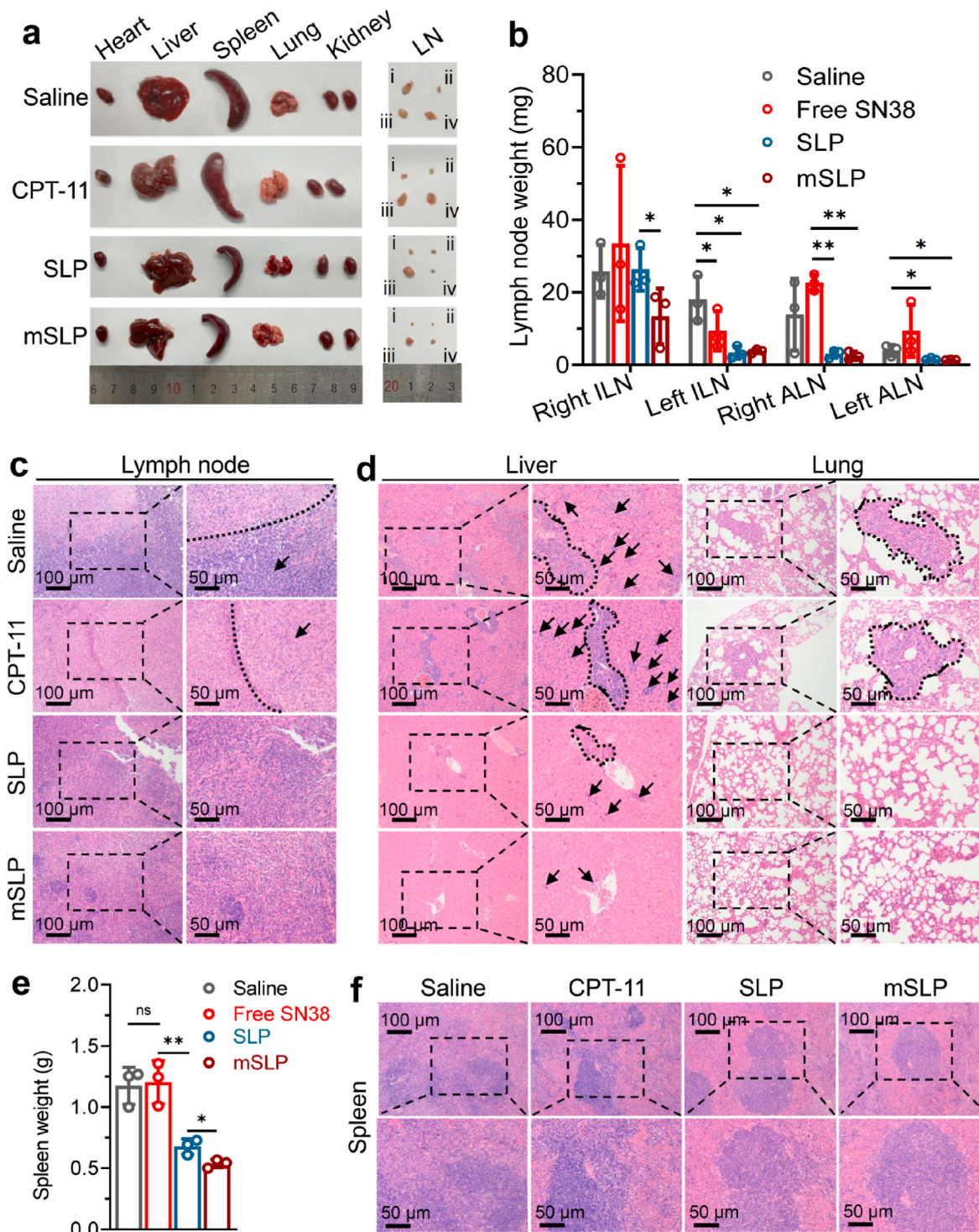


**Fig. 8.** *In vivo* antimetastatic activity of bioadhesive nanacamptothecin in a 4T1 spontaneous metastasis model. (a) Representative images of major organs and lymph nodes excised from each treatment group. i) Right axillary lymph node; ii) left axillary lymph node; iii) right inguinal lymph node; iv) left inguinal lymph node. (b) Weights of lymph nodes from different groups (n = 3). ILN, inguinal lymph node; ALN, axillary lymph node. (c and d) Histological analysis of the right inguinal lymph node, liver, and lung using H&E staining. (e) Statistical histogram of spleen weights in each group (n = 3). (f) H&E staining of the spleen. Data are presented as the means ± SD. \*p < 0.05 and \*\*p < 0.01.

clearance of nanoparticles from the body [10,12]. More disappointingly, this stealthy nanocarrier design may impede tumor cell uptake and compromise treatment efficacy [42]. In the past decade, cell membrane-camouflaged biomimetic approaches have been proposed to tackle these challenges [43,44]. Macrophages are highly plastic innate immune cells that differentiate into two types: classically (M1) and

alternatively (M2) activated macrophages. M1-type macrophages exert a proinflammatory and antitumorigenic effect and target cancerous cells, while M2 macrophages possess anti-inflammatory activity and phenotypically similar to tumor-associated macrophages (TAMs) [45]. Hence, M1-type macrophage membranes are potentially useful to construct biomimetic drug delivery systems, escape immune recognition

and potentiate efficacy by extending circulation [23].

Another vital advantage of using natural macrophage membranes is that cell membrane components help to increase the adhesion of the biomimetic nanoparticles to cancer cells and thereby enhance tumor cell uptake. Extensive crosstalk occurs between M1-type macrophages and cancer cells. For example, macrophages expressing  $\alpha 4$ -integrin and  $\beta 1$ -integrin show tropism to tumor sites through interactions with VCAM-1 overexpressed on the breast cancer cell membrane [29,30]. Breast cancer was also found to secrete C-C chemokine ligand 2 (CCL2), a chemotactic signal that facilitates the recruitment of CCR2-positive macrophages [46,47]. Moreover, intercellular adhesion molecule-1 (ICAM-1), a cell surface transmembrane glycoprotein that is overexpressed in triple-negative breast cancer cells, favors macrophage infiltration and adhesion [48–50]. Therefore, we leveraged the power of the M1-type macrophage membrane to increase adhesion to tumor cells. Indeed, compared with nonadhesive PEGylated lipid nanoparticles, membrane cloaking facilitated the adherence of nanocamptothecin to cancer cells and thereby achieved higher cellular uptake.

The DNA topoisomerase I inhibitor SN38 is a potent chemotherapy whose function is impeded by its low aqueous solubility, easy hepatic inactivation, and high risk of systemic toxicity. The clinically approved prodrug CPT-11 only exhibits improved solubility but reduced bioavailability compared with its active metabolite SN38. Carboxylesterase is required to remove the dipiperidino group for SN38 release after intravenous administration, but the enzymatic conversion rate is generally very low (<8%) [51]. Several groups, including our group, have focused on the development of new delivery formulations for SN38 to mitigate the drawbacks of the clinical use of CPT-11 and attempted to improve the therapeutic outcomes. Distinct linker chemistries and pro-moieties have been tested for this purpose. Unlike physical encapsulation of the free drug, packaging of covalently tethered polymeric prodrug stably constrains the parent SN38 agent in the cell membrane-derived carrier. The resulting nanocamptothecin is capable of releasing active SN38 quantitatively in response to abundant intracellular esterase. Results from *in vitro* cell-based experiments showed that bioadhesive nanocamptothecin exhibited comparable cytotoxicity to free SN38 but significantly higher potency than CPT-11. A prodrug approach using covalent linker chemistry generally will reduce the drug potency *in vitro* relative to its free drug form because an additional release step from nanotherapies and subsequent bond cleavage are required to restore the activity. Encouragingly, we did not observe the compromised potency *in vitro*, presumably due to enhanced adhesion and uptake by tumor cells.

In a preclinical mouse model of orthotopic and metastatic 4T1 breast cancer, substantial antitumor activity was observed after treatment with nanocamptothecin compared with the clinically approved drug CPT-11. Notably, cell membrane decoration facilitated more pronounced intratumor accumulation and eventually yielded more potent antitumor activity. Specifically, in adhesive mSLP-treated mice, the primary tumors were smaller and metastatic foci in organs such as the liver and lungs were less frequently observed than in mice treated with nonadhesive SLP therapy. Furthermore, no statistically significant variations in body weight were observed, indicating good safety profiles of nanoparticles.

## 5. Conclusion

In this study, we have described a nanotherapeutic platform based on a polymer-conjugated cytotoxic camptothecin prodrug with an esterase-activatable linkage, and a cell membrane cloaking approach. Our experimental results suggest the feasibility and augmented benefits of membrane-camouflaged nanocamptothecin for the systemic treatment of metastatic TNBC. The present cell-derived nanotherapeutics encapsulated a covalently conjugated agent, which rendered the prodrug stable in the blood circulation and improved cancer-targeting and therapeutic efficacy. Finally, because many anticancer active compounds are not compatible with the cell membrane approach, we foresee

that the prodrug strategy and biomimetic formulation have high potential utility for the creation of more potent nanomedicines.

## Data availability statement

The data are available from the corresponding author (wanghx@zju.edu.cn) on reasonable request.

## Ethics approval

All animal studies were conducted in accordance with the National Institute Guide for the Care and Use of Laboratory Animals. The experimental protocols were approved by the Ethics Committee of the First Affiliated Hospital, Zhejiang University School of Medicine.

All authors have contributed to this work and approved the manuscript for submission to Bioactive Materials.

## CRediT authorship contribution statement

**Kangkang Ying:** Investigation, Methodology, Formal analysis, Investigation, Visualization, Writing – original draft. **Yifeng Zhu:** Methodology, Investigation, Visualization, Validation. **Jianqin Wan:** Methodology, Investigation, Visualization, Validation. **Chenyue Zhan:** Methodology, Validation. **Yuchen Wang:** Methodology, Formal analysis, Visualization. **Binbin Xie:** Formal analysis, Supervision, Funding acquisition. **Peirong Xu:** Formal analysis, Visualization. **Hongming Pan:** Formal analysis, Visualization. **Hangxiang Wang:** Conceptualization, Methodology, Formal analysis, Writing – review & editing, Supervision, Funding acquisition.

## Declaration of competing interest

The authors declare that they have no known competing financial interests or personal relationships that could have appeared to influence the work reported in this paper.

## Acknowledgments

This study was supported by grants from Zhejiang Provincial Natural Science Foundation of China (LR19H160002), National Natural Science Foundation of China (82073296 and 81773193), and Research Project of Jinan Microecological Biomedicine Shandong Laboratory (JNL-2022010B). We thank the technical assistance from the Center of Cryo-Electron Microscopy (CEEM), Zhejiang University, for TEM analysis.

## Appendix A. Supplementary data

Supplementary data to this article can be found online at <https://doi.org/10.1016/j.bioactmat.2022.06.013>.

## References

- [1] L.R. Baden, H.M. El Sahly, B. Essink, K. Kotloff, S. Frey, R. Novak, D. Diemert, S. A. Spector, N. Roupael, C.B. Creech, J. McGettigan, S. Khetan, N. Segall, J. Solis, A. Brosz, C. Fierro, H. Schwartz, K. Neuzil, L. Corey, P. Gilbert, COVE Study Group, Efficacy and safety of the mRNA-1273 SARS-CoV-2 vaccine, *N. Engl. J. Med.* 384 (5) (2021) 403–416.
- [2] Safety and immunogenicity study of 2019-nCoV Vaccine (mRNA-1273) to prevent SARS-CoV-2 Infection, *ClinicalTrials.gov Identifier: NCT04283461*. Available from: <https://clinicaltrials.gov/ct2/show/NCT04283461>.
- [3] D. Peer, J.M. Karp, S. Hong, O.C. FaroKHzad, R. Margalit, R. Langer, Nanocarriers as an emerging platform for cancer therapy, *Nat. Nanotechnol.* 2 (12) (2007) 751–760.
- [4] C. Gottstein, G. Wu, B.J. Wong, J.A. Zasadzinski, Precise quantification of nanoparticle internalization, *ACS Nano* 7 (6) (2013) 4933–4945.
- [5] N. Bertrand, J. Wu, X. Xu, N. Kamaly, O.C. Farokhzad, Cancer nanotechnology: the impact of passive and active targeting in the era of modern cancer biology, *Adv. Drug Deliv. Rev.* 66 (2014) 2–25.
- [6] E. Blanco, H. Shen, M. Ferrari, Principles of nanoparticle design for overcoming biological barriers to drug delivery, *Nat. Biotechnol.* 33 (9) (2015) 941–951.

- [7] J.S. Suk, Q.G. Xu, N. Kim, J. Hanes, L.M. Ensign, PEGylation as a strategy for improving nanoparticle-based drug and gene delivery, *Adv. Drug Deliv. Rev.* 99 (2016) 28–51.
- [8] S. Peng, B. Ouyang, Y. Men, Y. Du, Y. Cao, R. Xie, Z. Pang, S. Shen, W. Yang, Biodegradable zwitterionic polymer membrane coating endowing nanoparticles with ultra-long circulation and enhanced tumor photothermal therapy, *Biomaterials* 231 (2020), 119680.
- [9] I. Hamad, O. Al-Hanbali, A.C. Hunter, K.J. Rutt, T.L. Andresen, S.M. Moghimi, Distinct polymer architecture mediates switching of complement activation pathways at the nanosphere-serum interface: implications for stealth nanoparticle engineering, *ACS Nano* 4 (11) (2010) 6629–6638.
- [10] K. Yu, B.F.L. Lai, J.H. Foley, M.J. Krisinger, E.M. Conway, J.N. Kizhakkedathu, Modulation of complement activation and amplification on nanoparticle surfaces by glycopolymer conformation and chemistry, *ACS Nano* 8 (8) (2014) 7687–7703.
- [11] V.P. Vu, G.B. Gifford, F. Chen, H. Benasutti, G. Wang, E.V. Groman, R. Scheinman, L. Saba, S.M. Moghimi, D. Simberg, Immunoglobulin deposition on biomolecule corona determines complement opsonization efficiency of preclinical and clinical nanoparticles (vol 14, pg 260, 2019), *Nat. Nanotechnol.* 14 (3) (2019), 298–298.
- [12] M. Pannuzzo, S. Esposito, L.P. Wu, J. Key, S. Aryal, C. Celia, L. di Marzio, S. M. Moghimi, P. Decuzzi, Overcoming nanoparticle-mediated complement activation by surface PEG pairing, *Nano Lett.* 20 (6) (2020) 4312–4321.
- [13] C.M. Hu, L. Zhang, S. Aryal, C. Cheung, R.H. Fang, L. Zhang, Erythrocyte membrane-camouflaged polymeric nanoparticles as a biomimetic delivery platform, *Proc. Natl. Acad. Sci. U.S.A.* 108 (27) (2011) 10980–10985.
- [14] C.M. Hu, R.H. Fang, K.C. Wang, B.T. Luk, S. Thamphiwatana, D. Dehaini, P. Nguyen, P. Angsantikul, C.H. Wen, A.V. Kroll, C. Carpenter, M. Ramesh, V. Qu, S.H. Patel, J. Zhu, W. Shi, F.M. Hofman, T.C. Chen, W. Gao, K. Zhang, L. Zhang, Nanoparticle biointerfacing by platelet membrane cloaking, *Nature* 526 (7571) (2015) 118–121.
- [15] R.H. Fang, C.M. Hu, B.T. Luk, W. Gao, J.A. Copp, Y. Tai, D.E. O'Connor, L. Zhang, Cancer cell membrane-coated nanoparticles for anticancer vaccination and drug delivery, *Nano Lett.* 14 (4) (2014) 2181–2188.
- [16] W. Lei, C. Yang, Y. Wu, G. Ru, X. He, X. Tong, S. Wang, Nanocarriers surface engineered with cell membranes for cancer targeted chemotherapy, *J. Nanobiotechnol.* 20 (1) (2022) 45.
- [17] A. Parodi, N. Quattrocchi, A.L. van de Ven, C. Chiappini, M. Evangelopoulos, J. O. Martinez, B.S. Brown, S.Z. Khaled, L.K. Yazdi, M.V. Enzo, L. Isenhardt, M. Ferrari, E. Tasciotti, Synthetic nanoparticles functionalized with biomimetic leukocyte membranes possess cell-like functions, *Nat. Nanotechnol.* 8 (1) (2013) 61–68.
- [18] Z. Chen, P. Zhao, Z. Luo, M. Zheng, H. Tian, P. Gong, G. Gao, H. Pan, L. Liu, A. Ma, H. Cui, Y. Ma, L. Cai, Cancer cell membrane-biomimetic nanoparticles for homologous-targeting dual-modal imaging and photothermal therapy, *ACS Nano* 10 (11) (2016) 10049–10057.
- [19] Q. Zhao, X. Sun, B. Wu, Y. Shang, X. Huang, H. Dong, H. Liu, W. Chen, R. Gui, J. Li, Construction of homologous cancer cell membrane camouflage in a nano-drug delivery system for the treatment of lymphoma, *J. Nanobiotechnol.* 19 (1) (2021) 8.
- [20] T. Meng, R. Jiang, S. Wang, J. Li, F. Zhang, J.H. Lee, J. Jiang, M. Zhu, Stem cell membrane-coated Au-Ag-PDA nanoparticle-guided photothermal acne therapy, *Colloid. Surf. B-Biointerf.* 192 (2020), 111145.
- [21] Y. Zhai, Y. Ma, B. Pang, J. Zhang, Y. Li, Y. Rui, T. Xu, Y. Zhao, Z. Qian, Y. Gu, S. Li, A cascade targeting strategy based on modified bacterial vesicles for enhancing cancer immunotherapy, *J. Nanobiotechnol.* 19 (1) (2021) 434.
- [22] Y. Ding, Y. Li, Z. Sun, X. Han, Y. Chen, Y. Ge, Z. Mao, W. Wang, Cell-derived extracellular vesicles and membranes for tissue repair, *J. Nanobiotechnol.* 19 (1) (2021) 368.
- [23] Y.Q. Xia, L. Rao, H.M. Yao, Z.L. Wang, P.B. Ning, X.Y. Chen, Engineering macrophages for cancer immunotherapy and drug delivery, *Adv. Mater.* 32 (40) (2020), e2002054.
- [24] T. Kang, Q. Zhu, D. Wei, J. Feng, J. Yao, T. Jiang, Q. Song, X. Wei, H. Chen, X. Gao, J. Chen, Nanoparticles coated with neutrophil membranes can effectively treat cancer metastasis, *ACS Nano* 11 (2) (2017) 1397–1411.
- [25] M. Kang, J. Hong, M. Jung, S.P. Kwon, S.Y. Song, H.Y. Kim, J.R. Lee, S. Kang, J. Han, J.H. Koo, J.H. Ryu, S. Lim, H.S. Sohn, J.M. Choi, J. Doh, B.S. Kim, T-cell-mimicking nanoparticles for cancer immunotherapy, *Adv. Mater.* 32 (39) (2020), e2003368.
- [26] R. Trivedi, U.B. Kompella, Nanomicellar formulations for sustained drug delivery: strategies and underlying principles, *Nanomedicine* 5 (3) (2010) 485–505.
- [27] Y. Wang, H. Xie, K. Ying, B. Xie, X. Chen, B. Yang, J. Jin, J. Wan, T. Li, W. Han, S. Fang, H. Wang, Tuning the efficacy of esterase-activatable prodrug nanoparticles for the treatment of colorectal malignancies, *Biomaterials* 270 (2021), 120705.
- [28] J.M. Suski, M. Lebidzinska, A. Wojtala, J. Duszynski, C. Giorgi, P. Pinton, M. R. Wieckowski, Isolation of plasma membrane-associated membranes from rat liver, *Nat. Protoc.* 9 (2) (2014) 312–322.
- [29] Q. Chen, X.H. Zhang, J. Massague, Macrophage binding to receptor VCAM-1 transmits survival signals in breast cancer cells that invade the lungs, *Cancer Cell* 20 (4) (2011) 538–549.
- [30] Q. Chen, J. Massague, Molecular pathways: VCAM-1 as a potential therapeutic target in metastasis, *Clin. Cancer Res.* 18 (20) (2012) 5520–5525.
- [31] A.B.E. Attia, C. Yang, J.P.K. Tan, S.J. Gao, D.F. Williams, J.L. Hedrick, Y.Y. Yang, The effect of kinetic stability on biodistribution and anti-tumor efficacy of drug-loaded biodegradable polymeric micelles, *Biomaterials* 34 (12) (2013) 3132–3140.
- [32] G. Koopman, C.P. Reutelingsperger, G.A. Kuijten, R.M. Keehnen, S.T. Pals, M. H. van Oers, Annexin V for flow cytometric detection of phosphatidylserine expression on B cells undergoing apoptosis, *Blood* 84 (5) (1994) 1415–1420.
- [33] J.F. Pizzolato, L.B. Saltz, The camptothecins, *Lancet* 361 (9376) (2003) 2235–2242.
- [34] Y. Pommier, Drugging topoisomerases: lessons and challenges, *ACS Chem. Biol.* 8 (1) (2013) 82–95.
- [35] A. Lesniak, A. Salvati, M.J. Santos-Martinez, M.W. Radomski, K.A. Dawson, C. Aberg, Nanoparticle adhesion to the cell membrane and its effect on nanoparticle uptake efficiency, *J. Am. Chem. Soc.* 135 (4) (2013) 1438–1444.
- [36] A. Akinc, G. Battaglia, Exploiting endocytosis for nanomedicines, *Cold Spring Harbor Perspect. Biol.* 5 (11) (2013) a016980.
- [37] N. Nagai, F. Ogata, H. Otake, Y. Nakazawa, N. Kawasaki, Energy-dependent endocytosis is responsible for drug transcorneal penetration following the instillation of ophthalmic formulations containing indomethacin nanoparticles, *Int. J. Nanomed.* 14 (2019) 1213–1227.
- [38] A.C. Garrido-Castro, N.U. Lin, K. Polyak, Insights into molecular classifications of triple-negative breast cancer: improving patient selection for treatment, *Cancer Discov.* 9 (2) (2019) 176–198.
- [39] J. Cuzick, M. Dowsett, S. Pineda, C. Wale, J. Salter, E. Quinn, L. Zabaglo, E. Mallon, A.R. Green, I.O. Ellis, A. Howell, A.U. Buzdar, J.F. Forbes, Prognostic value of a combined estrogen receptor, progesterone receptor, Ki-67, and human epidermal growth factor receptor 2 immunohistochemical score and comparison with the genomic health recurrence score in early breast cancer, *J. Clin. Oncol.* 29 (32) (2011) 4273–4278.
- [40] T.O. Nielsen, S. Leung, D.L. Rimm, A. Dodson, B. Acs, S. Badve, C. Denkert, M. J. Ellis, S. Fineberg, M. Flowers, H.H. Kreipe, A.V. Laenkholm, H. Pan, F. M. Penault-Llorca, M.Y. Polley, R. Salgado, I.E. Smith, T. Sugie, J. Bartlett, L. M. McShane, D.F. Hayes, Assessment of Ki67 in breast cancer: recommendations from the international Ki67 in breast cancer working group, *JNCI-J. Natl. Cancer Inst.* 103 (22) (2011) 1656–1664.
- [41] B.A. Pulaski, S. Ostrand-Rosenberg, Reduction of established spontaneous mammary carcinoma metastases following immunotherapy with major histocompatibility complex class II and B7.1 cell-based tumor vaccines, *Cancer Res.* 58 (7) (1998) 1486–1493.
- [42] S. Tenzer, D. Docter, J. Kuharev, A. Musyanovych, V. Fetz, R. Hecht, F. Schlenk, D. Fischer, K. Kiouptsi, C. Reinhardt, K. Landfester, H. Schild, M. Maskos, S. K. Knauer, R.H. Stauber, Rapid formation of plasma protein corona critically affects nanoparticle pathophysiology, *Nat. Nanotechnol.* 8 (10) (2013) 772–U1000.
- [43] B.T. Luk, L.F. Zhang, Cell membrane-camouflaged nanoparticles for drug delivery, *J. Contr. Release* 220 (2015) 600–607.
- [44] X. Zhen, P.H. Cheng, K.Y. Pu, Recent advances in cell membrane-camouflaged nanoparticles for cancer phototherapy, *Small* 15 (1) (2019), e1804105.
- [45] M. Locati, G. Curtale, A. Mantovani, Diversity, mechanisms, and significance of macrophage plasticity, *Annu. Rev. Pathol.* 15 (2020) 123–147.
- [46] B.Z. Qian, J. Li, H. Zhang, T. Kitamura, J. Zhang, L.R. Campion, E.A. Kaiser, L. A. Snyder, J.W. Pollard, CCL2 recruits inflammatory monocytes to facilitate breast-tumour metastasis, *Nature* 475 (7355) (2011), 222–U129.
- [47] L.M. Arendt, J. McCready, P.J. Keller, D.D. Baker, S.P. Naber, V. Seewaldt, C. Kuperwasser, Obesity promotes breast cancer by CCL2-mediated macrophage recruitment and angiogenesis, *Cancer Res.* 73 (19) (2013) 6080–6093.
- [48] Y. Usami, K. Ishida, S. Sato, M. Kishino, M. Kiryu, Y. Ogawa, M. Okura, Y. Fukuda, S. Toyosawa, Intercellular adhesion molecule-1 (ICAM-1) expression correlates with oral cancer progression and induces macrophage/cancer cell adhesion, *Int. J. Cancer* 133 (3) (2013) 568–578.
- [49] C. Schröder, I. Witzel, V. Müller, S. Krenkel, R.M. Wirtz, F. Jänicke, U. Schumacher, K. Milde-Langosch, Prognostic value of intercellular adhesion molecule (ICAM)-1 expression in breast cancer, *J. Cancer Res. Clin. Oncol.* 137 (8) (2011) 1193–1201.
- [50] C. Rosette, R.B. Roth, P. Oeth, A. Braun, S. Kammerer, J. Ekblom, M.F. Denissenko, Role of ICAM-1 in invasion of human breast cancer cells, *Carcinogenesis* 26 (5) (2005) 943–950.
- [51] V.J. Venditto, E.E. Simanek, Cancer therapies utilizing the camptothecins: a review of the in vivo literature, *Mol. Pharmacol.* 7 (2) (2010) 307–349.